Low Electric Field Drift Tube Ion Mobility Analysis for Atmospheric Pressure Plasma

Keith Nealson M. PENADO, Allen Vincent B. CATAPANG and Motoi WADA

Graduate School of Science and Engineering, Doshisha University, Kyotanabe, Kyoto 610-0321, Japan

(Received 18 February 2023 / Accepted 14 March 2023)

A low voltage compact ion mobility spectrometer type charged particle analyzer is being investigated to test the performance for diagnostics of ion/electron transport in an atmospheric pressure environment. The 44 mm diameter, 53 mm long device consists of a mesh gated shutter, a 35 mm long drift region, and an end-plate detector. By applying a cyclic positive bias followed by a negative bias to the shutter region, subsequent attraction and expulsion of charged species is observed with the applied voltage less than 100 V. Mesh size dependence of the shutter gated current at the detector shows that across 0, 30, 100, and 200 mesh sizes, the 30 mesh size realized the transport of the most number of ions towards the detector. This mesh size also presents a well-defined current-time derivative which allows the measurement of ion mobilities in electric fields with the intensity less than 33.3 V/cm. Analysis of peaks observed after the onset of the positive phase shows the presence of O^+ ions in the swarm with a reported experimental mobility of $K_0 = 2.97\,\mathrm{cm}^2/\mathrm{Vs}$.

Keywords: ion mobility spectrometry, plasma diagnostics, atmospheric pressure plasma

DOI: 10.1585/pfr.18.1406029

1. Introduction

Ion mobility spectrometry (IMS) is a common method for the analysis of ions in a given swarm under ambient pressures. It has found applications ranging from explosives [1, 2], and drug detection [3], to air quality [4], and food quality analysis [5]. The process is defined to be an electrophoretic method designed to separate ions in a given swarm according to their size and charges. The basis of IMS lies in the analysis of the ions' inherent mobilities, K, as they move through an inert gas field of a constant electric field, E, with a drift velocity, v_d [6]. The mobility is calculated from the ions' charge (q), the buffer gas density (N), the reduced mass (μ), the temperature-dependent collision integral ($\Omega^{(1,1)}(T_{eff})$), and the correction factor (α). The effective temperature (T_{eff}), which characterizes the energy in the center-of-mass frame, is used to describe the mobility coefficient [7].

$$K = \frac{3q}{8N}\left(\frac{\pi}{2\mu k_b T_{eff}}\right)^{\frac{1}{2}} \frac{1+\alpha}{\Omega^{(1,1)}(T_{eff})}. \quad (1)$$

Several types of IMS technologies are available such as Travelling Wave IMS (TWIMS) [8, 9], Trapped IMS (TIMS) [10, 11], Field Assymetric IMS (FAIMS) [12], and Drift tube IMS (DTIMS) [13], of which is regarded to be the classic IMS model. A DTIMS device contain three major elements to achieve ion species analysis; the separation region, the drift region, and the detection region. The separation region consists of an ion gate to trigger the entrance of ions into the spectrometer. Two of the most common gates are the Bradbury-Nielsen gate (BNG) [14], and the Tyndall gate (TG) [15]. Both gating mechanisms involve the creation of an electric field between two sets of thin wires to allow the passage of a singular charged species to flow into the spectrometer.

After the ions pass through the separation region, they are accelerated through the drift region by a near uniform electric field. In typical DTIMS devices, the electric field could be described as low ($E \sim 5$ - 10 kV/cm) to high ($E > 100$ kV/cm) [16]. The requirements for high electric field and precisely controlled carrier gas flow often make the design and operation of DTIMS complicated. In this study, a DTIMS configuration is employed for ambient measurement of electrical charge transport in the absence of a buffer gas flow at low electric fields with intensities less than 33.3 V/cm.

2. Experimental Details

The schematic diagram of the ion mobility analyzer coupled to the ion source is presented in Fig. 1. Charged species are generated using a 13.56 MHz RF powered capacitively coupled atmospheric pressure plasma jet source [17]. The plasma source operates at an input power of 40 W with the minimum reflected power down to 1.8 W. Argon gas was introduced into the plasma source at a flow rate of 5 liters per minute. The aperture of the mobility spectrometer is placed in direct contact with the plasma source. Three main components: the bipolar pulse gated shutter, the drift region, and the detector constitute the spectrometer.

author's e-mail: cyjf3303@mail4.doshisha.ac.jp

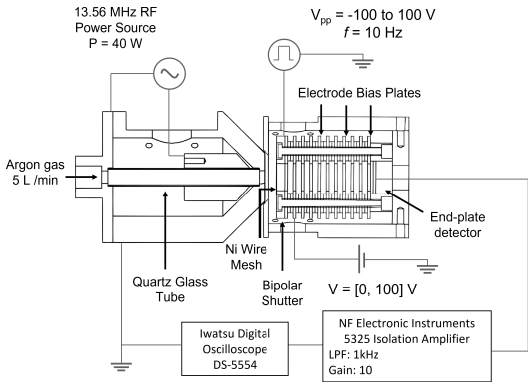

Fig. 1 Schematic diagram of the RF capacitively coupled atmospheric pressure plasma source coupled to the drift tube spectrometer.

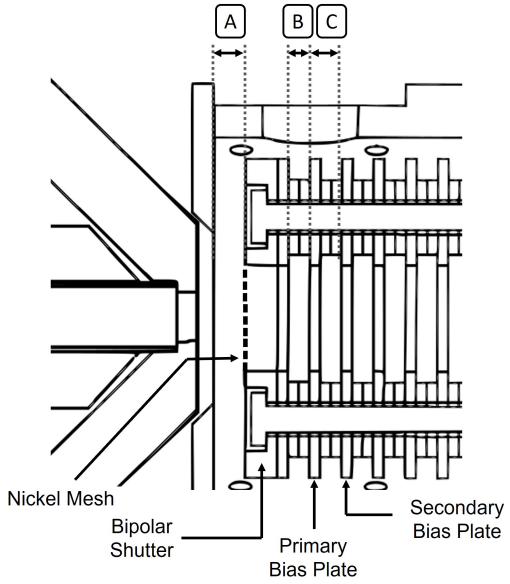

Fig. 2 Schematic diagram of the spectrometer around the shutter region. The following regions correspond to a series of potential variations to realize charge transport to the detector: (A) d = 5 mm, V_i = 0 V, V_f = ±100 V, (B) d = 2 mm, V_i = ± 100 V, $V_f = V_{Bias}$, (C) d = 3 mm, $V_i = V_{Bias}$, V_f = 0.9 (V_{Bias}), where d is the length of the region, V_i is the initial potential, and V_f is the final potential.

The plasma from the source fills the 10 mm diameter and 5 mm deep volume of the shutter electrode. A sheet of 99% Ni wire mesh (Nilaco Co.) with mesh sizes of 30, 100, and 200 corresponding to wire diameters of 0.15, 0.1, and 0.05 mm and aperture sizes of 600, 150, and 75 μm respectively is placed at the front side of the shutter electrode in direct contact with the source plasma. The 10 mm diameter 35 mm long drift region starts from the mesh and ends at the detector. A closer view of the area around the shutter region is described in Fig. 2. A uniform DC electric field is created in the drift region without any flow of a buffer gas. The 12 mm diameter copper detector plate is stationed at the end of the drift region inside a Faraday shield.

A function generator (EZ Digital Co. Ltd. DGF-6003) coupled to an amplifier (Turtle Industries Co. Ltd. T-HVA01) drives the voltage of the Al shutter electrode with respect to the outer cylinder of the RF plasma source at the ground potential. The shutter driving voltage has a square waveform of alternating polarity switching between ±100 V at a frequency of 10 Hz. The potential of the primary bias plate is kept at constant voltage, V_{Bias}, to accelerate positive ions toward the detector with a DC voltage source (TEXIO PSW-360H800) up to 100 V. The succeeding 10 copper bias plates, separated by a 1 MΩ resistor, are positioned 3 mm from each other to realize a drift space of constant electric field an intensity of $E = V_{Bias}/3$ cm. This structure results to a potential drop of 10% of the applied voltage for every succeeding bias plate.

The charged particle swarm transported through the drift region reaches the detector plate to generate electrical current signal. An isolation amplifier (NF Electronic Instruments 5325) with 1 kHz low pass filter converts the current signals collected at the plate detector to voltage signals. The oscilloscope (IWATSU DS-5554 Digital Oscilloscope) trace is recorded at an average of 32 samples with a sampling rate of 5 MS/s. Measurements were taken at 1 atm ambient air pressure at an average room temperature of 300 K.

3. Experimental Results

3.1 Positive field transport

The detector current measured for varying mesh sizes are shown in Fig. 3. In all figures, the shutter electrode changes potential from −100 V to +100 V at time t = 50 ms. In the case where there was no mesh, or 0 mesh condition, no significant change was observed when the shutter potential was changed. However, with the addition of a mesh, a phase-locked signal was clearly observed. A typical ion transport signal, time-of-flight peak after opening/closing the shutter, is observed at an applied potential to the first electrode, V_{Bias} = 50, 100 V. To elucidate the time-of-flight peak, the raw oscilloscope trace, and its corresponding Gaussian fitted profiles for the 30 mesh 100 V shutter voltage condition are shown in Fig. 4. As the shutter voltage changes at t = 50 ms, the resolution of the spectrum estimated from the delay time divided by the full width at the half maximum can be as small as one as shown in Fig. 4. The time-of-flight signal peak appeared to arrive later as the V_{Bias} was reduced to 50 V for the 30 mesh shutter.

Another important parameter that changes characteristically against V_{Bias} is the DC detector current. In the 0 mesh condition, the detector current increased as V_{Bias} was set more positive. For the cases that the spectrometer was operated with the 30 mesh shutter electrodes at 50 and 100 V V_{Bias}, the detector current stayed constant over the cycle except the time-of-flight pulse signal. The mea-

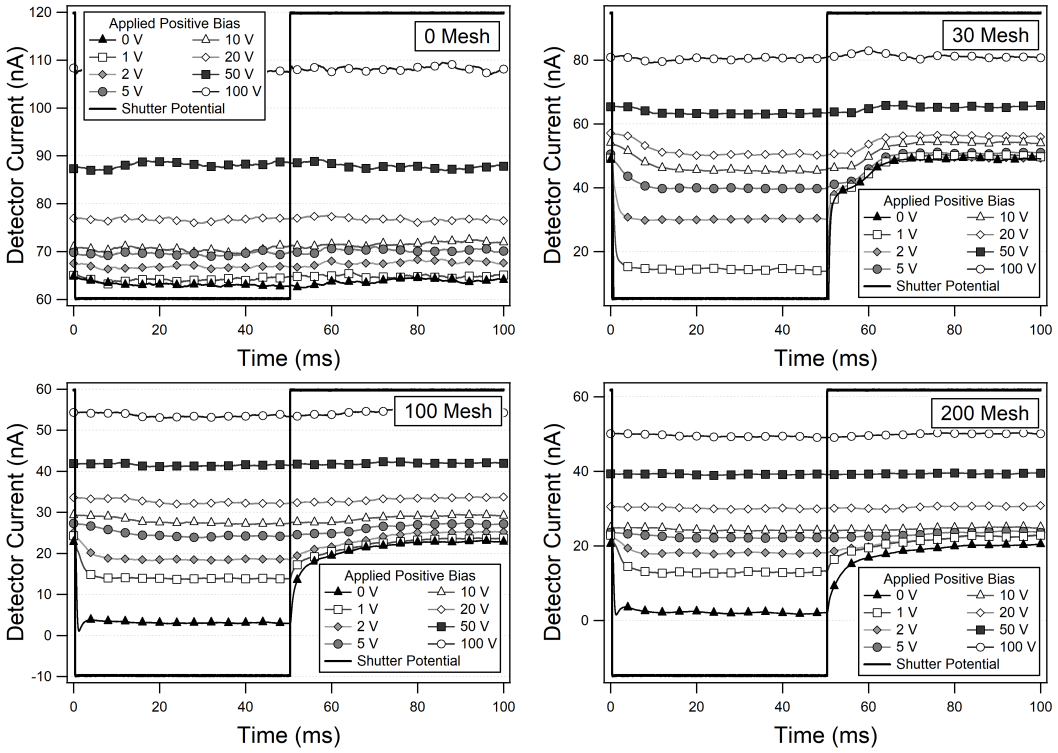

Fig. 3 Charge transport in a positive field through 0, 30, 100, and 200 mesh sizes. The solid black line corresponds the shutter potential switching from −100 V to +100 V at t = 50 ms. The applied bias from 1 - 100 V corresponds to an electric field of 0.33 - 33.33 V/cm in the drift region. The scale of the 30 Mesh diagram has been modified to elucidate the positive phase transport. Points were skipped to improve the visualization of data.

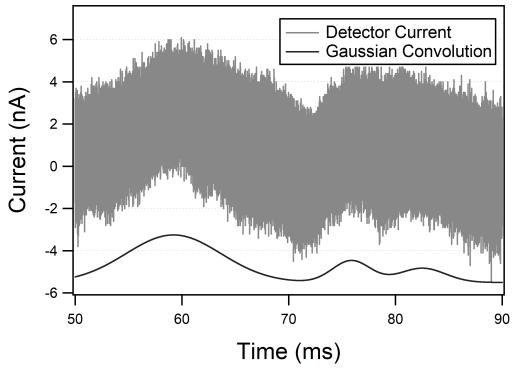

Fig. 4 Observed positive phase detector current through a 30 mesh at an applied bias of 100 V. Gaussian peak fitting of the detector current was performed using the MultiPeak function in IgorPro V6.04.

sured detector current reached the quasi-steady values toward the phase end of the square wave plateau as V_{Bias} was set smaller than 20 V. The values of detector current signal for these steady-state conditions are plotted in Figs. 5 (a) and 5 (b) by subtracting the detector current at the corresponding phase of the cycle with the V_{Bias} = 0 condition. As it is expected, the detector current decreases as the mesh size of the shutter electrode increases. This tendency of current magnitude is consistent to the transparency of the mesh screen. Neither Fig. 5 (a) for the negative bias phase nor Fig. 5 (b) for the positive bias phase exhibits linear dependence against V_{Bias} and the ion flux reaching the detector is not solely determined by the velocity proportional to the electric field intensity in the drift region.

3.2 Time response of the detector current

The mesh size of the shutter electrode not only changes the detector current amplitude but also the time response of the detector current signal. Comparing signals of 100 mesh and 200 mesh, the detector current for 200 mesh rises more slowly than the current shuttered by 100 mesh. As the mesh size was decreased down to 30, the time constant for the change in detected current at the onset of the shutter voltage change became larger. The waveform exhibited asymmetry in this mesh condition between the positive and negative shutter voltages became more clearly. Larger time constants were observed when the shutter voltage was changed from negative to positive. Meanwhile, the smaller time constant of the detector current waveform as the shutter voltage starts to send ions to drift space indicates the contribution of electron swarm in the detector system. This characteristic behavior: fast time response of the detector current by the shutter voltage change was confirmed when the polarity of the electric field in the drift tube region was reversed.

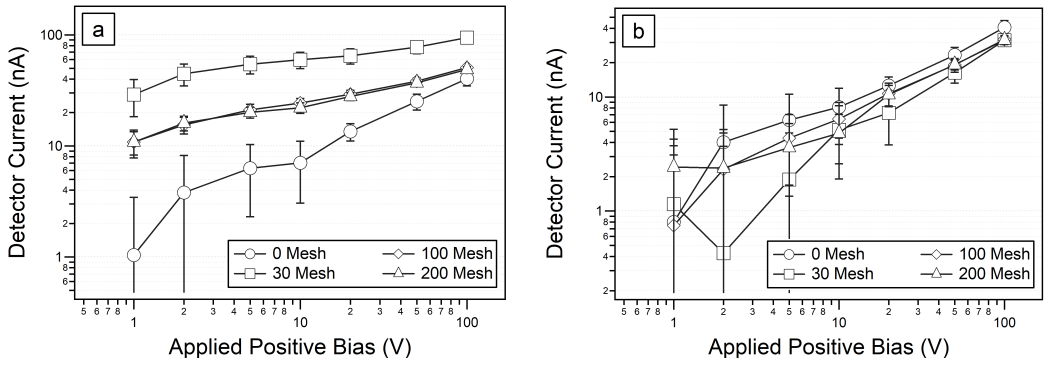

Fig. 5 The effect of increasing electric fields on the steady state currents observed when the shutter potential is (a) negative, and (b) positive across varying mesh sizes. The current is measured relative to the baseline steady state current at $V_{Bias} = 0$ V. The experiment was repeated three times with the values in (a), and (b) reporting an average standard deviation of 4.74 nA, and 3.02 nA respectively.

4. Discussion

A typical detector current from the spectrometer is presented in Fig. 6 for a 30 mesh shutter DTIMS operation. Negative and positive detector current phases corresponding to the polarity of the applied shutter potential can be categorized as transition regions, R1, R3, and a steady state regions R2, R4, as indicated in the figure. These time domains are R1: 0 - 20 ms, R2: 20 - 40 ms, R3: 50 - 80 ms, and R4: 80 - 95 ms, respectively. The time dependent change of the current can be more clearly observed. The usual operation region for classical DTIMS without a gas flow at low drift field intensity is R3. Unlike the typical DTIMS, the current device is operated with extremely low electric field intensity. The peak observed in the region R3 is analyzed to determine the corresponding mobility. Due to the phase-asymmetry observed in this region, typical phase subtraction does not result in the elucidation of the time-of-flight peak. Instead, the time-of-flight peak in this region is elucidated by obtaining the point at which the current-time derivative is maximized [18].

When the electric field intensity is large enough, the velocity that can be determined from the time-of-flight is proportional to the ion mobility, K. The peaks appearing in Fig. 4 correspond to the mobilities $K = 12, 4.1, 3.3\,\mathrm{cm^2/Vs}$ for the peaks observed at $t = 59.21$, 75.87, and 82.52 ms, respectively. However, the field intensity of the present system is low compared with traditional DTIMS and the ion mobility is calculated assuming the drift velocity equation $v_d = v_0 + KE$ [19]. A linear regression analysis was made for the peak observed in the current-time derivative spectrometer signal in a 30 mesh transport at $t = 55$ - 80 ms, and $V_{Bias} = 5$ - 50 V. The slope of the regression shows a mobility value of $K = 3.0\,\mathrm{cm^2/Vs}$, and an initial velocity $v_0 = 350$ cm/s. The mobility data are compared with the reported reduced mobilities normalized to 1 atm and 273 K to determine the ion species.

The observed initial velocity is much higher than what is typically expected from atmospheric pressure plasma

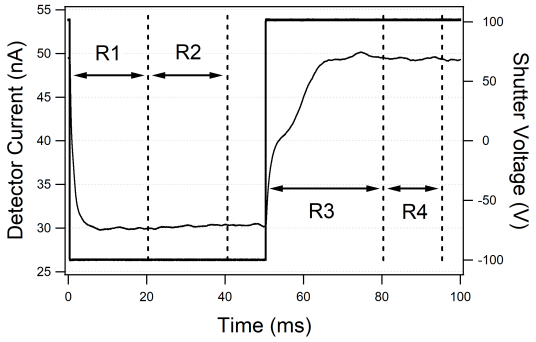

Fig. 6 Charge transport in a 30 mesh shutter with $V_{Bias} = 2$ V. The solid black line corresponds to the shutter potential. The negative phase is composed of R1, and R2, while R3 and R4 correspond to the positive phase. The negative phase starts at 0 ms, while the positive phase starts at 50 ms. The odd, and even number regions correspond to the transition and the steady state regions respectively.

[20]. In our experimental geometry, positive ions can acquire some velocity as the mesh electrode bias changes from −100 V to +100 V. During the time the mesh is biased at −100 V, positive ions can form cloud of positive space charge around mesh. As the electrode potential is raised to +100 V, an electric field in the vicinity of the mesh surface accelerates ions toward the drift field. The existence of collisions should diminish this initial velocity, but it can be close to an acoustic speed of air. The high initial velocity could also be attributed to the high recombination rate of Ar^+ in atmospheric pressure condition as high as $3 \times 10^{-13} \sim 4 \times 10^{-14}\,\mathrm{m^3/s}$ which diminishes slow ions reaching the drift region [21].

The third peak measured at $V_{Bias} = 100$ V, and the peak observed at $V_{Bias} = 5$ - 50 V correspond to the reduced mobilities, $K_0 = 3.0$ and $2.7\,\mathrm{cm^2/Vs}$, respectively. These peaks can be attributed to the presence of O^+ in the swarm. The presence of oxygen in the source plasma was confirmed by optical emission spectroscopy. The emission

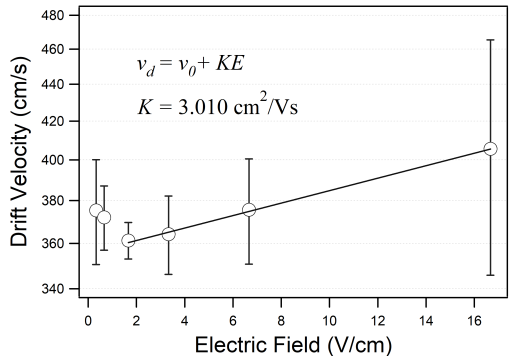

Fig. 7 Linear regression of the drift velocities corresponding to the current-time derivative peak of the observed spectrometer signal in a 30 mesh transport at low electric fields from t = 55 - 80 ms. Error bars indicate the standard deviation of the drift velocities over three experimental trials. V_{Bias} = 5 - 50 V corresponds to an average electric field of 1.67 to 16.67 V/cm.

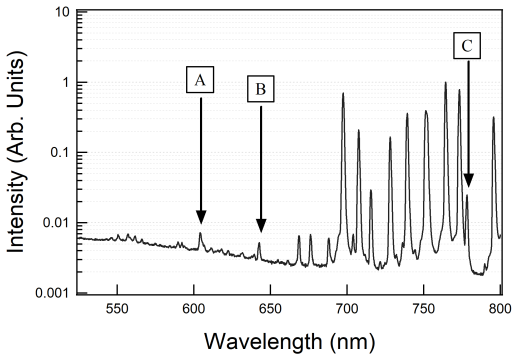

Fig. 8 Optical emission spectra of the CCP plasma source at a flow rate of 5 L/min and an input power of 40 W. The indicated peaks in the spectra (A) 604 nm, (B) 645 nm, and (C) 777 nm peaks of atomic O I in the plasma correspond to the most probable transitions levels present in the plasma. Other peaks present in the spectra correspond to the transition levels of Ar I [22, 23].

spectrum in the visible range shown in Fig. 8 clearly indicates the O I line spectra at 604, 645 and 777 nm wavelengths. It is likely that other ions such as N_2^+, CO^+, H_2O^+, and O_2^+ can be attributed to the aforementioned peaks since they share a similar range of mobility [7, 16]. However, the presence of these molecular ions from the optical emission spectrum have yet to be confirmed.

The difficulty in local plasma measurement at V_{Bias} < 2 V leaves the reason for observing complicated behavior of the DC detector current shown in Fig. 5 (b), and the drift velocity shown in Fig. 7 as an unanswered question. Larger current was recorded at 1 V bias voltage, except the case that the mesh was removed. The electrostatic acceleration between the mesh to the first electrode of the drift region should not change drastically by elevating the bias voltage from 1 to 2 V. The possible explanation can be made by combining ion space charge and the volume/surface recombination rate in the drift tube region. Further study on the local plasma parameters and their spatial distribution must be necessary to elucidate the physics of low field operation of a drift tube.

5. Conclusion

An operation principle of a low-electric-field gas-flow-free drift tube ion mobility spectrometer has been studied for diagnostics of an atmospheric pressure plasma. With the addition of a mesh at the shutter electrode, phase dependent signals depending upon the electric field intensity in the drift region were obtained. Results show that across the 30, 100, and 200 mesh sizes, ion transport across the 30 mesh results to the highest charge collection at the detector. The time derivative of the detector current shows that the 30 mesh size exhibits the sharpest peak among the mesh sizes making it preferred for mobility measurements in low electric fields. Analysis of ion transport in a drift field shows the presence of a peak in the time-of-flight spectrum corresponding to the mobility of 3.0 cm^2/Vs, and 2.7 cm^2/Vs measured at an applied bias of 100, and 5 - 50 V respectively. The peak can be attributed to the drift of O^+ ions, while the optical emission spectrum shows O I line spectra.

The operation by inducing a bipolar square wave pulse produces the time dependent ion drift current. The detector current waveform changes in accordance with the electric field intensity that can be controlled with the electric voltage less than 100 V. By setting up a proper model that fully explains the effect due to the mesh size and the initial swarm velocity, mobility spectrum and other plasma parameters can be obtained from the time dependent detector current of a low-electric-field gas-flow-free drift tube ion mobility spectrometer

[1] R.G. Ewing, D.A. Atkinson, G.A. Eiceman and G.J. Ewing, Talanta **54**, 515 (2001).
[2] M. Makinen, M. Nousiainen and M. Sillanpaa, Mass Spectrom. Rev. **30**, 940 (2011).
[3] J.R. Verkouteren and J.L. Staymates, Forensic Sci. **206**, 190 (2010).
[4] G.A. Eiceman, E.G. Nazarov, B. Tadjikov and R.A. Miller, Field Analyt. Chem. Technol. **4**, 297 (2000).
[5] W. Vautz, D. Zimmermann, M. Hartmann, J.I. Baumbach, J. Nolte and J. Jung, Food Addit. Contam. **11**, 1064 (2006).
[6] L.A. Viehland and E.A. Mason, Ann. Phys. **91**, 499 (1975).
[7] L.A. Viehland and E.A. Mason, At. Data Nucl. Data Tables **60**, 37 (1995).
[8] A.A. Shvartsburg and R.D. Smith, Anal. Chem. **80**, 9699 (2008).
[9] K. Giles, S.D. Pringle, K.R. Worthington, D. Little, J.L. Wildgoose and R.H. Bateman, Rapid. Comm. Mass Spectrom. **18**, 2401 (2004).
[10] D.R. Hernandez, J.D. DeBord, M.E. Ridgeway, D.A. Kaplan, M.A. Park and F.F. Lima, Analyst **139**, 1913 (2014).
[11] F.A. Fernandez-Lima, D.A. Kaplan and M.A. Park, Rev.

Sci. Instrum. **82**, 126106 (2011).
[12] I.A. Buryakov, E.V. Krylov, E.G. Nazarov and U. Kh. Rasulev, Int. J. Mass Spectrom. Ion Processes **128**, 143 (1993).
[13] D.C. Collins and M.L. Lee, Anal. Bional. Chem. **372**, 66 (2002).
[14] N.E. Bradbury and R.A. Nielsen, Phys. Rev. **49**, 388 (1936).
[15] A.M. Tyndall and C.F. Powell, Proc. R. Soc. Lond. A **129**, 162 (1930).
[16] H.W. Ellis, R.Y. Pai, E.W. McDaniel, E.A. Mason and L.A. Viehland, At. Data Nucl. Data Tables **17**, 177 (1976).
[17] M.C.C. Lacdan and M. Wada, Plasma Fusion Res. **11**, 2401015 (2016).
[18] T.C.O. Haver, Anal. Proc. **19**, 22 (1982).
[19] Y.P. Raizer, *Gas Discharge Physics* (Springer, Verlag Berlin Heidelberg, 1991) p.20.
[20] Y. Kim, J. Jeong, G. Han, D. Jin, J. Kim and G. Cho, *Plasma diffusion in the atmospheric pressure plasma jets* (2011 Abstracts IEEE International Conference on Plasma Science, Chicago, IL, 2011) p.1-1.
[21] M. Suzuki and A. Kanzawa, Kagaku Kogaku Ronbunshu **4**, 381 (1978) [In Japanese].
[22] A. Kramida, Y. Ralchenko, J. Reader and NIST ASD Team, *NIST Atomic Spectra Database (ver 5.10)*. (NIST, Gaithersburg, 2022).
[23] N.S. Braithwaite, Plasma Sources Sci. Technol. **9**, 517 (2000).